applied sciences

MDPI

Article

Local Space-Charge Memory and Grounded-Electrode Transient Response in a Needle–Plane Air Gap Under Polarity Reversal

Shiwei Du [1], Li Zhang [1], Yiyan Zhang [1], Kai Chang [1], Ikromjon Rakhmonov Usmonovich [2], Nurbek Nurullo ugli Kurbonov [2] and Hui Zhong [1,*]

[1] School of Electrical Engineering, Shandong University, Jinan 250061, China
[2] Power Engineering Faculty, Tashkent State Technical University, Tashkent 100095, Uzbekistan
* Correspondence: zhonghui@sdu.edu.cn

Abstract

Polarity reversal changes not only the instantaneous electric field in a needle–plane air gap but also the subsequent field–particle coupling through the charged-particle distribution established before reversal. For a configuration in which the grounded needle and grounded lower plate share the same return path, it remains unclear to what extent this local history-dependent state is transferred to the complete grounded conductor and its externally measurable current. Here, a two-dimensional axisymmetric electrostatic model (ES) and a drift–diffusion–reaction–Poisson–discharge-fluid model (EDIS) were established for a 50 mm needle–plane air gap. Positive-to-negative (P2N)/negative-to-positive (N2P) reversals and history-retained/history-reset (H/R) controls were used to separate the effects of reversal path and pre-existing charged-particle state. Over the tested 0–2τ reset-hold range, the representative near-tip electron density in H remained approximately 15–16% higher than that in the corresponding R case, whereas the H/R conductor-integrated response of the complete common-ground assembly was indistinguishable at the present numerical resolution. Outer-domain analysis further showed that for the representative 15 kV case in the 300 mm reference domain, the EDIS and ES common-ground integrated responses differed by approximately 3.3%. Experimentally, P2N and N2P reversals were repeated at 5, 10, and 15 kV, yielding 120 events. The main common-ground current pulse increased with voltage magnitude and maximum voltage slew rate, and the median event-level Pearson correlation with signed dV/dt was approximately 0.989. Different capacitance-baseline constructions yielded central residual-integral levels of approximately 18–19%; after multiplicity correction, the 15 kV fixed-window absolute integral was the direction-sensitive terminal metric with the strongest statistical support. Under the investigated conditions—a nominal 0.5 mm tip radius, 50 mm gap, approximately 3 ms reversal time, and weak-discharge regime—the reversal path and particle history primarily reorganize the near-tip charged-particle state, whereas the dominant scale of the common-ground transient remains closely associated with the applied-voltage variation and the capacitive response of the system.

Keywords: needle–plane air gap; polarity reversal; space charge; displacement current; grounded electrode

Academic Editor: Roberto Zivieri

Received: 25 July 2026
Revised: 19 August 2026
Accepted: 25 August 2026
Published: 27 August 2026

1. Introduction

A needle–plane air gap produces a strongly nonuniform electric field within a confined region because of the small radius of curvature at the needle tip. It is therefore widely used to investigate corona inception, space-charge evolution, streamer propagation, and external electrical responses [1–4]. Under steady DC conditions, positive- and negative-polarity discharges differ in electron supply, attachment, photoionization, secondary-electron emission, and space-charge distribution [4–7]. When the applied voltage reverses polarity, the electrons and positive and negative ions formed before reversal do not disappear instantaneously. Consequently, the post-reversal local state may depend not only on the instantaneous voltage, but also on the voltage trajectory and the charged-particle state inherited from the preceding stage.

Previous studies have commonly characterized polarity-dependent behavior using the electric field, particle density, discharge morphology, propagation velocity, or current pulses near the needle tip. Although these quantities describe local discharge processes, they cannot be directly equated with the current measured in the common grounding conductor [8–13]. The measured current is a system-level response that may contain displacement current generated by changes in electric displacement, induced current associated with space-charge motion, collection current produced when charged particles reach an electrode, and contributions from device parasitics, switching coupling, and the dynamic response of the measurement chain [7,14–17]. Thus, even substantial changes in the electron density or space charge near the needle tip may produce only a limited relative change in the integrated conductor charge or in the measured common-ground current. This local-to-system distinction is particularly relevant to the driven-upper-plate/common-ground needle–lower-plate configuration used here because high-field protrusions such as grounded rods, lightning rods, and wind-turbine receptors exposed to thunderstorm background fields may likewise develop localized corona and space charge, whereas the externally monitored quantity is determined by the complete grounding or down-conductor path [18–20].

In repetitively pulsed and repetitive discharges, the memory effect generally refers to the influence of residual electrons, ions, metastable species, residual conductivity, or surface charge from a preceding discharge on a subsequent discharge [21–25]. In numerical studies, the contribution of the pre-existing charged-particle state can be isolated by retaining or resetting the particle distributions while keeping the subsequent voltage function unchanged. The reset case used here is an idealized numerical control and does not represent an experimental operation capable of instantaneously removing all charged particles from the gap. The P2N/N2P comparison simultaneously involves the reversal direction, the voltage trajectory, and the polarity history, whereas the H/R comparison is used for a fixed reversal direction to assess the influence of the pre-existing charged-particle state.

Recent numerical studies of thunderstorm-field polarity reversal have shown that corona charge established during the preceding voltage stage can influence the subsequent opposite-polarity discharge [10], while investigations of positive and negative corona from grounded rods have demonstrated that the polarity and magnitude of the background field affect the local corona state [6,12]. In parallel, studies of repetitively pulsed and repetitive discharges have established that residual electrons, ions, space charge, or surface charge can modify a subsequent discharge [21–24]. These bodies of work provide the physical basis for polarity effects, reversal history, and discharge memory. However, for the common-ground configuration considered here, a specific cross-scale question remains unresolved, i.e., whether near-tip differences induced by the reversal path or by a pre-existing charged-particle state are transferred with a comparable relative magnitude to the charge integrated over the complete grounded conductor and ultimately, to the externally measurable common-ground transient.

To address this question, the present study combines three observational levels within the same needle–plane configuration: the near-tip electron/space-charge state, the charge

https://doi.org/10.3390/app16178536

integrated over the grounded conductor formed by the needle and lower plate, and the experimentally measured common-ground current. Specifically, we (1) establish two numerical levels, ES and EDIS, to distinguish the structural capacitive reference from the grounded-boundary response obtained when charged-particle transport is included; (2) use paired P2N/N2P and H/R cases to examine the effects of reversal path and pre-existing particle state, respectively; (3) test the stability of key numerical observables against mesh refinement, time-integration settings, and outer-domain size; and (4) combine synchronized voltage/common-ground-current measurements from 5 to 15 kV with repeated-event statistics to assess the dependence of the terminal response on voltage slew rate, voltage excursion, and reversal direction.

2. Materials and Methods

2.1. Model Configuration

A two-dimensional axisymmetric needle–plane air-gap model was established, as shown in Figure 1. The upper plate was the driven electrode, whereas the needle was located at the center of the lower plate and electrically connected to it so that both formed a common-ground assembly. The shortest axial distance from the needle tip to the upper plate was 50 mm. The needle height was 20 mm, and both the needle-body radius and the nominal tip radius were 0.5 mm. The experimental electrode and the numerical model used the same nominal geometry. Before and after each group of tests, the needle tip and adjacent metal surfaces were inspected for visible pitting, erosion, or mechanical damage; the needle was replaced if macroscopic changes that could alter the local field distribution were observed. The physical upper-plate radius was kept at 200 mm. Numerical outer-air radii of 200, 250, and 300 mm were used to assess the effect of the artificial outer boundary on conductor-integrated quantities; the physical electrode dimensions, local tip geometry, and common-ground integration boundary were unchanged among the three models. Air was specified at 300 K and 101,325 Pa, with N_2 and O_2 volume fractions of 0.80 and 0.20, respectively.

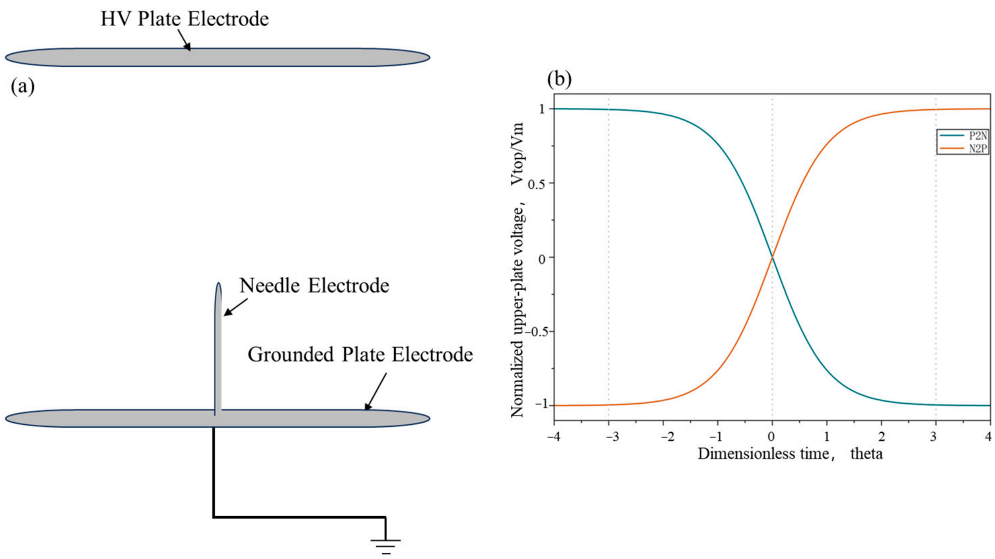

Figure 1. (**a**) Two-dimensional axisymmetric geometry and electrical topology of the driven upper plate and common-ground needle/lower-plate assembly; the tip-to-upper-plate gap is 50 mm, and the nominal tip radius is 0.5 mm. (**b**) Normalized P2N and N2P voltage-reversal trajectories; $\theta = -3$, 0, and +3 denote the representative pre-reversal, zero-crossing, and post-reversal states, respectively. The vertical dashed lines in (**b**) indicate the representative states at $\theta = -3$, 0, and +3.

A mirrored polarity-reversal voltage with a magnitude of 15 or 25 kV was applied to the upper plate:

$$V_{\text{top}}(t) = sV_{\text{m}}\tanh\left(\frac{t - t_{\text{rev}}}{\tau_{\text{rev}}}\right) \quad (1)$$

where V_{m} is the voltage magnitude, t_{rev} is the voltage zero-crossing time, and $\tau_{\text{rev}} \approx 1.36$ ms is the characteristic time of the reversal. The corresponding 10–90% voltage transition time is t_10–90 ≈ 2.99 ms. For s = −1, the voltage changes from positive to negative polarity (P2N); for s = +1, it changes from negative to positive polarity (N2P). To compare different cases at equivalent stages of the reversal, the dimensionless time is defined as

$$\theta = \frac{t - t_{\text{rev}}}{\tau_{\text{rev}}} \quad (2)$$

The dimensionless times θ = −3, 0, and +3 were selected to represent the pre-reversal, zero-crossing, and post-reversal states, respectively. At $\theta = \pm 3$, $|V_{\text{top}}| \approx 0.995\ V_{\text{m}}$. For the matched instantaneous-voltage comparison, the P2N and N2P states were selected on opposite branches of the reversal trajectory.

To distinguish the effect of the instantaneous voltage from that of the pre-existing charged-particle state, history-retained (H) and history-reset (R) cases were defined. The H case was integrated continuously from the pre-polarization stage through the reversal stage and therefore inherited the electron, positive-ion, and negative-ion distributions established before reversal. The R case used exactly the same subsequent voltage function as did the corresponding H case, but the charged-species number densities were restored at the prescribed reset time to the baseline values $n_{\text{e},0} = 1.0 \times 10^9$ m^{-3}, $n_{\text{p},0} = 2.0 \times 10^9$ m^{-3}, and $n_{\text{n},0} = 1.0 \times 10^9$ m^{-3}. Reset-hold times of 0, 1τ, and 2τ were additionally examined, while the subsequent voltage trajectory was kept unchanged. Thus, the H/R comparison for a given reversal direction isolates the influence of the pre-existing charged-particle state, whereas the P2N–R/N2P–R comparison at a matched instantaneous voltage evaluates reversal-path dependence.

2.2. Electrostatic and Discharge-Fluid Numerical Models

An electrostatic model and a discharge-fluid model were used. The electrostatic model provided a grounded-boundary reference without charged-particle transport or space-charge feedback. No free charge was assigned in the air domain, and the electric potential and field satisfy

$$\nabla \cdot (\varepsilon \nabla \varphi) = 0 \quad (3)$$

$$\mathbf{E} = -\nabla \varphi \quad (4)$$

where φ is the electric potential, E is the electric-field strength, and $\varepsilon = \varepsilon_0 \varepsilon_r$ is the permittivity. The relative permittivity of air was set to 1.

The discharge-fluid model consisted of a coupled drift–diffusion–reaction–Poisson system for electrons, positive ions, and negative ions and was implemented using the Electric Discharge interface in COMSOL Multiphysics 6.4 (COMSOL AB, Stockholm, Sweden). Such fluid models have been widely used for numerical studies of needle–plane corona and streamer discharges in air [1,4,9–11,26–30], while the software implementation followed the Electric Discharge Module documentation [31]. The electrostatic model is denoted as ES, and the discharge-fluid model established with the Electric Discharge interface is denoted as EDIS. The continuity equation for charged species S is

$$\frac{\partial n_s}{\partial t} + \nabla \cdot \mathbf{\Gamma}_s = S_s \quad (5)$$

The particle-number flux is

$$\mathbf{\Gamma}_s = z_s \mu_s n_s \mathbf{E} - D_s \nabla n_s \quad (6)$$

where n_s, μ_s, and D_s are the number density, mobility, and diffusion coefficient of species s, respectively; z_s denotes the charge sign in the drift term, with $z_s = +1$ for positive ions and $z_s = -1$ for electrons and negative ions; and S_s is the net production rate of species S.

The space-charge density is determined by the electron, positive-ion, and negative-ion populations:

$$\rho = e(n_+ - n_e - n_-) \quad (7)$$

where e is the elementary charge magnitude. The electric potential in the discharge-fluid model satisfies

$$\nabla \cdot (\varepsilon \nabla \varphi) = -\rho \quad (8)$$

The space charge generated by charged-particle transport and reactions therefore modifies the local electric field, while the field in turn controls electron and ion drift and reaction rates, resulting in a self-consistent field–particle coupling.

The EDIS model employs a drift–diffusion–reaction formulation under the local-field approximation for three effective charged species: electrons, positive ions, and negative ions. Electron transport coefficients and the impact-ionization and electron-attachment coefficients are functions of the reduced electric field E/N, while diffusion is treated using the Einstein relation. Comparable drift–diffusion–reaction–Poisson fluid formulations have been widely used for needle–plane corona and streamer discharges in air [1,4,9–11,26–30]. The volume reactions include impact ionization, two-body electron attachment, three-body electron attachment, electron–positive-ion recombination, and positive–negative-ion recombination. The positive- and negative-ion mobilities are 2.34 and 2.70 $cm^2\ V^{-1}\ s^{-1}$, respectively, with pressure scaling, and both recombination coefficients are $2 \times 10^{-7}\ cm^3\ s^{-1}$. Electron mobility, impact-ionization coefficients, and electron-attachment coefficients are taken from the E/N-dependent material functions used in the model [4,27,31]. Photoionization is represented by a three-term Helmholtz approximation, with p_p = 150 Torr, p_q = 30 Torr, and ξ = 0.06, following the work of Refs. [32–36]. Charged species on the upper plate, grounded needle, and grounded lower plate are subject to the No Diffusive Flux boundary condition [31]. The principal quantitative inputs are summarized in Table 1.

Table 1. Quantitative transport, reaction, photoionization, initialization, and electrode-boundary settings of the EDIS model.

Parameter/Process	Value or Expression	Unit	Source/Implementation
Gas state	T = 300 K; p = 101,325 Pa; N_2/O_2 = 0.80/0.20	—	Present model
Electron mobility	$\mu_e = w_e(E/N)/\max(\lvert E \rvert, 1\ V\ m^{-1})$	$m^2\ V^{-1}\ s^{-1}$	E/N-dependent material function [4,27,31]
Positive-ion mobility	$\mu_p = 2.34(p_0/p)$, p_0 = 1 atm	$cm^2\ V^{-1}\ s^{-1}$	Present model; [4,27,31]
Negative-ion mobility	$\mu_n = 2.70(p_0/p)$, p_0 = 1 atm	$cm^2\ V^{-1}\ s^{-1}$	Present model; [4,27,31]
Diffusion	Einstein relation	—	[4,27,31]
Impact ionization	$e + M \rightarrow 2e + X^+$; $\alpha = \alpha_N(E/N)N$	m^{-1}	[4,27,31]
Two-/three-body attachment	$e + O_2 \rightarrow X^-$; $e + O_2 + M \rightarrow X^- + M$	—	$\eta_{2N}(E/N)N + \eta_{3NN}(E/N)N^2$ [4,27,31]
Recombination	$\beta_{ep} = \beta_{pn} = 2 \times 10^{-7}$	$cm^3\ s^{-1}$	Present model; [4,27]
Photoionization	Three-term Helmholtz; p_p = 150 Torr; p_q = 30 Torr; ξ = 0.06	—	[31–36]

Table 1. *Cont.*

Parameter/Process	Value or Expression	Unit	Source/Implementation
Initial/reset densities	$n_e = 1 \times 10^9$; $n_p = 2 \times 10^9$; $n_n = 1 \times 10^9$	m^{-3}	Present model
Charged-species electrode BC	No Diffusive Flux	—	Active on all three electrodes [28]

2.3. Integrated Grounded-Electrode Quantities and Experimental Waveform Diagnostics

In the experiment, the needle electrode and lower plate were connected to the same grounding conductor. Accordingly, the numerical integration boundary Γ_g included both the needle surface and the lower-plate surface, but excluded the upper plate, outer-air boundary, and symmetry axis. This conductor combination is referred to as the grounded-electrode assembly. For the two-dimensional axisymmetric model, the corresponding three-dimensional integrated charge is defined as

$$Q_{\text{ground}}(t) = 2\pi \int_{\Gamma_g} r(\mathbf{D} \cdot \mathbf{n})\mathrm{d}l \tag{9}$$

where r is the radial coordinate, dl is the boundary line element of the two-dimensional axisymmetric model, and the boundary normal follows the outward normal of the model domain. The numerical current derived from the time variation of the integrated charge of the grounded-electrode assembly is defined as

$$I_{\text{ground}}(t) = \frac{\mathrm{d}Q_{\text{ground}}(t)}{\mathrm{d}t} \tag{10}$$

I_{ground} is the grounded-boundary displacement current derived from the temporal variation of the electric-displacement flux over the grounded-electrode assembly.

The electrostatic model yields Q_{ES}, whereas the discharge-fluid model yields Q_{EDIS}; both are evaluations of the same common-ground quantity Q_{ground} defined by Equation (9). Their signed relative discrepancy over the same reversal window is defined as

$$r_{\text{cross}} = \frac{Q_{\text{EDIS}} - Q_{\text{ES}}}{|Q_{\text{ES}}|} \times 100\% \tag{11}$$

The quantity r_{cross} evaluates the change in the grounded-boundary integrated charge caused by introducing charged-particle transport relative to the electrostatic reference.

For a local quantity x, such as electron number density, space charge, or local electric field, the bounded relative difference between P2N/N2P or H/R cases is defined as

$$A = \frac{2(x_1 - x_2)}{|x_1| + |x_2| + \varepsilon} \tag{12}$$

where ε is a small positive number introduced to prevent division by zero. For the conductor-integrated common-ground quantity, the effects of mesh discretization, time integration, and solver settings are evaluated separately through the direct relative change of the same observable. For a calculation j in which only one numerical setting is changed, we define

$$\delta_Q^{(j)} = \frac{\left|Q_{\text{ground}}^{(j)} - Q_{\text{ground}}^{(\text{ref})}\right|}{\left|Q_{\text{ground}}^{(\text{ref})}\right|} \times 100\% \tag{13}$$

where $Q_{\mathrm{ground}}^{(\mathrm{ref})}$ is the common-ground integrated quantity obtained with the reference numerical setting, and $Q_{\mathrm{ground}}^{(j)}$ is the same quantity obtained after changing only one numerical setting. Mesh discretization, the BDF maximum allowed step, relative tolerance, and outer-air-domain size are evaluated separately; perturbations from different numerical sources are not collapsed into a single uncertainty index. The principal settings and their effects on Q_{ground} are summarized in Table 2.

Table 2. Numerical settings and sensitivity checks for the conductor-integrated grounded-boundary quantity.

Item	Setting/Perturbation	Quantitative Result
Mesh M0/M1/M2	2666/2807/2875 triangular elements	M0 → M1: 0.0208%; M1 → M2: 0.0160% in Q_{ground}
Degrees of freedom	M1: 10,987; M2: 11,277	Reported for refined meshes
Near-tip minimum element	2.5/1.25/0.625 µm	M0/M1/M2
Time integration	Adaptive BDF; maximum order 3	Internal step controlled by solver
Maximum-step sensitivity	$\tau_{\mathrm{rev}}/10 \rightarrow \tau_{\mathrm{rev}}/20$	No detectable Q_{ground} change at adopted reporting precision
Relative tolerance	$5 \times 10^{-4} \rightarrow 1 \times 10^{-4}$	Q_{ground} change < 10^{-6}%
Nonlinear/linear solver	Three segregated groups/MUMPS	Same solver sequence across compared cases
Outer-air radius	200/250/300 mm	Outer-domain dependence assessed at 15 kV

Note: The arrow (→) denotes a change from the reference setting to the refined setting used for the sensitivity check.

The experimental diagnostics were calculated from the corrected current I_{corr}(t). The absolute peak current, fixed-window absolute current integral, peak time, peak-time offset, and full width at half maximum were defined as follows:

$$I_{\mathrm{pk}} = \max_{t\in[t_1,t_2]}|I_{\mathrm{corr}}(t)| \tag{14}$$

$$Q_{\mathrm{win}} = \int_{t_1}^{t_2}|I_{\mathrm{corr}}(t)|\mathrm{d}t \tag{15}$$

$$t_{\mathrm{pk}} = \underset{t\in[t_1,t_2]}{\operatorname{argmax}}|I_{\mathrm{corr}}(t)| \tag{16}$$

$$\Delta t_{\mathrm{peak}} = t_{\mathrm{peak}} - t_{\mathrm{zero}} \tag{17}$$

$$|I_{\mathrm{corr}}(t_L)| = |I_{\mathrm{corr}}(t_R)| = \frac{I_{\mathrm{pk}}}{2} \tag{18}$$

$$\mathrm{FWHM} = t_R - t_L \tag{19}$$

Here, t_{zero} is the zero-crossing time of the measured voltage. The FWHM for both P2N and N2P was calculated from the absolute current waveform. Q_{win} quantifies the cumulative transient response within a fixed time window and is not equivalent to a signed net charge transfer.

To construct the fitted displacement-current baseline, the apparent capacitance for each event was estimated by least squares over the main-response fitting window [t_{f1}, t_{f2}]:

$$C_{\mathrm{app}} = \frac{\int_{t_{f1}}^{t_{f2}} I_{\mathrm{corr}}(t)\frac{\mathrm{d}V(t)}{\mathrm{d}t}\mathrm{d}t}{\int_{t_{f1}}^{t_{f2}}\left[\frac{\mathrm{d}V(t)}{\mathrm{d}t}\right]^2\mathrm{d}t} \tag{20}$$

$$I_{\mathrm{D,fit}}(t) = C_{\mathrm{app}}\frac{\mathrm{d}V(t)}{\mathrm{d}t} \tag{21}$$

$$I_{\mathrm{res}}(t) = I_{\mathrm{corr}}(t) - I_{\mathrm{D,fit}}(t) \tag{22}$$

The residual integral fraction after subtraction of the fitted displacement-current baseline is defined as

$$f_{\text{res}} = \frac{\int_{t_1}^{t_2} |I_{\text{res}}(t)|\,dt}{\int_{t_1}^{t_2} |I_{\text{corr}}(t)|\,dt} \times 100\% \quad (23)$$

Because C_{app} was obtained by fitting the voltage and current waveforms of the same event, f_{res} quantifies the deviation of the measured common-ground current from the best-fit displacement-current-type waveform.

2.4. Experimental Setup

The experimental system consisted of positive and negative DC high-voltage supplies (Suqian Boher High Voltage Power Supplies Co., Ltd., Suqian, China), a custom-built polarity-reversal switch, a current-limiting protective resistor, a custom-fabricated needle–plane electrode assembly, a high-voltage divider (Wuhan Guodian Xigao Electric Co., Ltd., Wuhan, China), a Rogowski coil (Rocoil Limited, Harrogate, UK), a digital storage oscilloscope (Tektronix, Inc., Beaverton, OR, USA), and a data-processing computer. The upper plate was connected to the polarity-reversal switch through the protective resistor. The needle electrode and lower plate were electrically connected and grounded through the same conductor. The Rogowski coil was installed around this common grounding conductor, and its output represented the total transient current passing through the measurement point of the grounded-electrode assembly.

The high-voltage-divider output was connected to oscilloscope channel CH1 to record the upper-plate voltage V(t), while the Rogowski-coil output was connected to CH2 to record the current in the common grounding conductor. Before formal testing, the amplitude response and timing response of the high-voltage divider and Rogowski-coil channels were calibrated. Both channels were sampled synchronously by the same oscilloscope, and their relative delay was corrected using a common calibration signal. All waveforms were referenced to the zero crossing of the measured CH1 voltage.

Tests were performed at voltage magnitudes of 5, 10, and 15 kV. P2N denotes reversal of the upper-plate voltage from $+V_{\text{m}}$ to $-V_{\text{m}}$, and N2P denotes reversal from $-V_{\text{m}}$ to $+V_{\text{m}}$. The polarity transition time was approximately 3 ms. Each combination of voltage magnitude and reversal direction was repeated independently 20 times. The fixed-window absolute current integral and peak-time offset were calculated using Equations (15) and (17), respectively. The same alignment method, integration window, filter bandwidth, and feature-extraction rules were applied to all tests.

All events were processed using the same analysis pipeline. The zero crossing of the measured upper-plate voltage on CH1 defined t = 0, and the CH2 baseline offset was corrected over the stable pre-event interval from −6.0 to −4.5 ms. Both channels were sampled synchronously at 1 MS/s. The voltage slew rate was obtained using a third-order Savitzky–Golay procedure with a nominal 101-point window; 51- and 201-point windows were used for filter-sensitivity checks.

For each event, C_app was determined by the zero-intercept least-squares form of Equation (20) over the fitting interval from −2.5 to +3.5 ms, excluding the main-response core from −0.25 to +1.25 ms. The residual integral defined by Equation (23) was evaluated over a fixed window from −3.0 to +4.0 ms. The nominal delay correction of CH2 relative to CH1 was 5 µs, and 0, 5, and 10 µs were used to test sensitivity to the delay treatment. The same baseline, filtering, fitting, integration, and delay-correction rules were applied to every voltage magnitude and reversal direction.

The arithmetic mean and sample standard deviation of the 20 repeated tests in each group were calculated as

$$\overline{x} = \frac{1}{N}\sum_{i=1}^{N} x_i \tag{24}$$

$$s_x = \sqrt{\frac{\sum_{i=1}^{N}(x_i - \overline{x})^2}{N-1}} \tag{25}$$

For each of the six voltage–direction groups (n = 20), group estimates are reported together with 95% confidence intervals. P2N/N2P comparisons were evaluated using Welch's tests, with Hedges' g reported as the standardized effect size, and the Holm procedure was applied across the predefined direction comparisons. For the 15 kV fixed-window absolute integral, which retained statistical support after multiplicity adjustment, a bootstrap 95% confidence interval for Hedges' g is additionally reported.

3. Numerical Results

3.1. Comparison of History-Reset Cases at the Same Instantaneous Positive Voltage

Figure 2 compares the near-tip field distributions for the 15 kV P2N–R and N2P–R cases at the same instantaneous positive voltage. P2N–R was sampled at θ = −3 and N2P–R at θ = +3; the upper-plate voltage at both instants was close to $+V_{\mathrm{m}}$. The two states, therefore, enable comparison of how different reversal paths affect the local charged-particle distribution under the same instantaneous applied voltage.

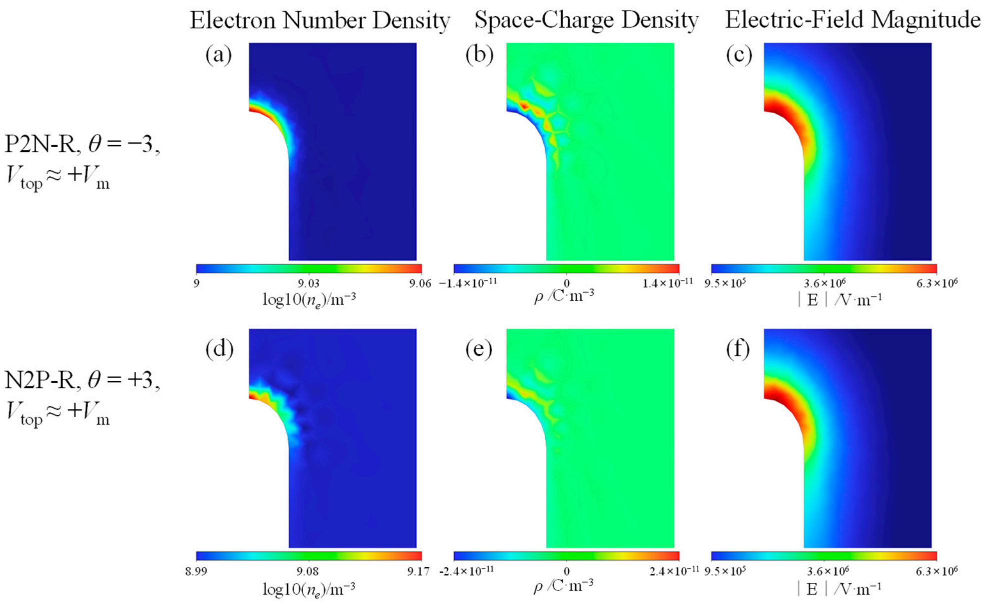

Figure 2. Near-tip field distributions for two history-reset reversal paths at the same instantaneous positive voltage at 15 kV: (**a**,**d**) electron number density; (**b**,**e**) space-charge density; and (**c**,**f**) electric-field magnitude.

In Figure 2a,d, the high-electron-density regions are concentrated near the needle surface and decay rapidly in the radial and axial directions. The electron number densities in both cases are on the order of 10^9 m^{-3}, and no continuous high-density channel extends from the needle tip to the upper plate. The high-electron-density region is more spatially continuous in P2N–R, whereas N2P–R exhibits stronger local nonuniformity near the needle tip. Although the two cases have the same instantaneous voltage, they occupy different stages of the trajectories leading to that voltage. P2N–R at θ = −3 corresponds to the positive-voltage stage before reversal, during which electron transport and production–loss processes near the tip have evolved continuously under a positive field, giving a smoother distribution. N2P–R at θ = +3 corresponds to field reconstruction after reversal from negative to positive polarity; electron drift, local ionization, attachment balance, and space-charge feedback are being readjusted, which produces a more nonuniform high-density region. Because the two reset cases use the same background charged-particle initial values, the difference reflects the effect of the post-reset voltage trajectory on the near-tip electron distribution.

Figure 2b,e show that space charge is likewise concentrated near the needle tip, while most of the gap remains approximately electrically neutral. Adjacent positive and negative space-charge regions occur in both cases, but their ranges and local contours differ. The space-charge ranges are approximately $\pm 1.4 \times 10^{-11}$ C m^{-3} for P2N–R and $\pm 2.4 \times 10^{-11}$ C m^{-3} for N2P–R, indicating that the reversal path changes the local electron and ion distributions near the needle tip.

Figure 2c,f show that, for both reversal paths, the maximum electric field is located near the needle surface and decays rapidly with distance from the tip. The high-field regions in P2N–R and N2P–R have similar spatial extents and overall contours, indicating that the dominant near-tip field structure is comparable under the same electrode geometry and instantaneous upper-plate voltage. By contrast, the electron-density and space-charge distributions in Figure 2a,b,d,e retain clearly different local organizations. Under the present conditions, the reversal-path effect is therefore expressed primarily through the spatial distribution of charged particles near the needle rather than through a large change in the dominant electric-field structure. The two history-reset paths thus exhibit comparable principal field structures at the same instantaneous voltage while retaining distinct near-tip electron and space-charge distributions, demonstrating path-dependence of the local charged-particle state.

3.2. Local Space-Charge Memory with a Retained Pre-Reversal Charged-Particle State

Figure 3 compares the H and R cases for the 15 kV P2N reversal at the same geometry and observation time, θ = +3. The only difference between the two cases is whether or not the charged-particle distribution from the preceding stage is inherited when the system enters the current voltage stage. The comparison, therefore, isolates the influence of the initial charged-particle state on the present local distribution.

In Figure 3a, the high-electron-density region in the H case forms a relatively continuous thin layer along the needle surface and extends into the adjacent gas. In Figure 3b, the electrons remain concentrated near the tip, but the high-density region is narrower and more spatially discrete. Figure 3c shows that the H − R electron-density difference is mainly positive at the needle surface and in the adjacent gas and reaches the order of 10^9 m^{-3}; it decreases rapidly outside the high-field region. Retaining the pre-existing charged-particle state therefore increases the near-tip electron density at the observation time, while the influence remains localized near the tip.

In Figure 3d,e, both H and R form adjacent positive and negative space-charge regions. The nonzero space-charge region is more extensive in H, and the positive and negative charge structures near the tip are more clearly separated. The H − R distribution in Figure 3f contains both positive and negative regions, indicating that history retention changes the magnitudes and relative positions of both positive and negative space charge rather than shifting the net charge of the entire region in a single direction.

At the same subsequent voltage trajectory and observation time, the H/R difference remains concentrated in the high-field region near the needle tip. Retaining the pre-reversal charged-particle state modifies the electron number density and the relative distributions of positive and negative space charge in this region, indicating a distinct local history-dependent charged-particle state in the model.

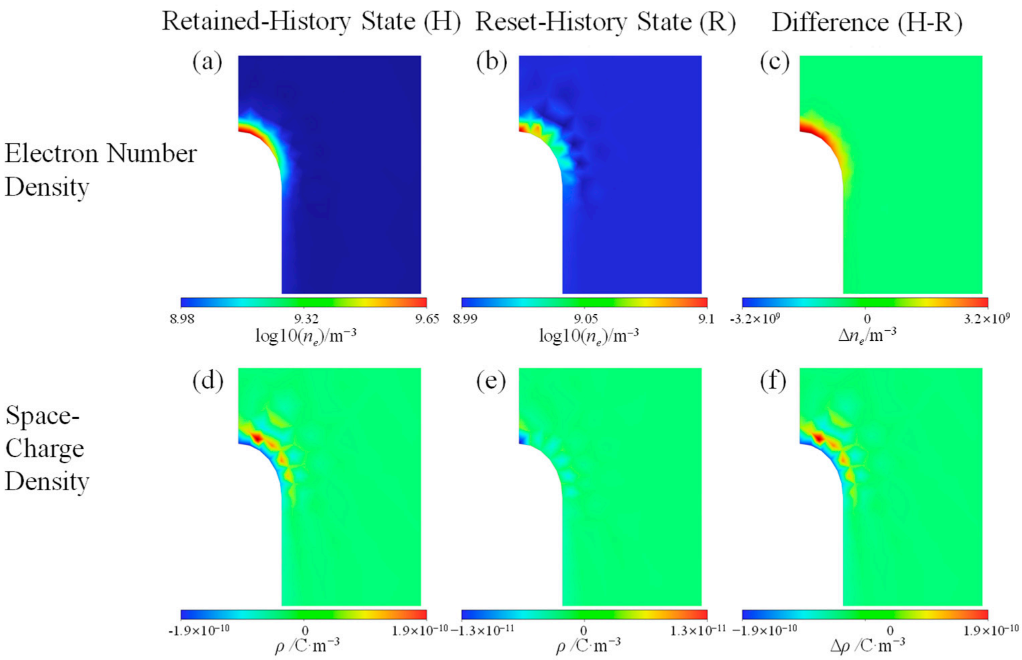

Figure 3. H/R comparison for the 15 kV P2N case at θ = +3. The first column shows the history-retained state H, the second the history-reset state R, and the third the H − R difference: (**a**,**b**) logarithmic electron-number-density distributions; (**c**) electron-number-density difference; (**d**,**e**) space-charge density; and (**f**) space-charge-density difference.

3.3. Outer-Domain Dependence of the Grounded-Boundary Integrated Charge

Figure 4 examines the effect of the artificial outer-air-domain size on the conductor-integrated common-ground response at 15 kV. Outer-air radii of 200, 250, and 300 mm were considered. The physical electrode dimensions, common-ground integration boundary Γ_g, local tip-mesh definition, comparison endpoints, and axisymmetric integration procedure were kept identical; only the radius of the surrounding air domain was changed.

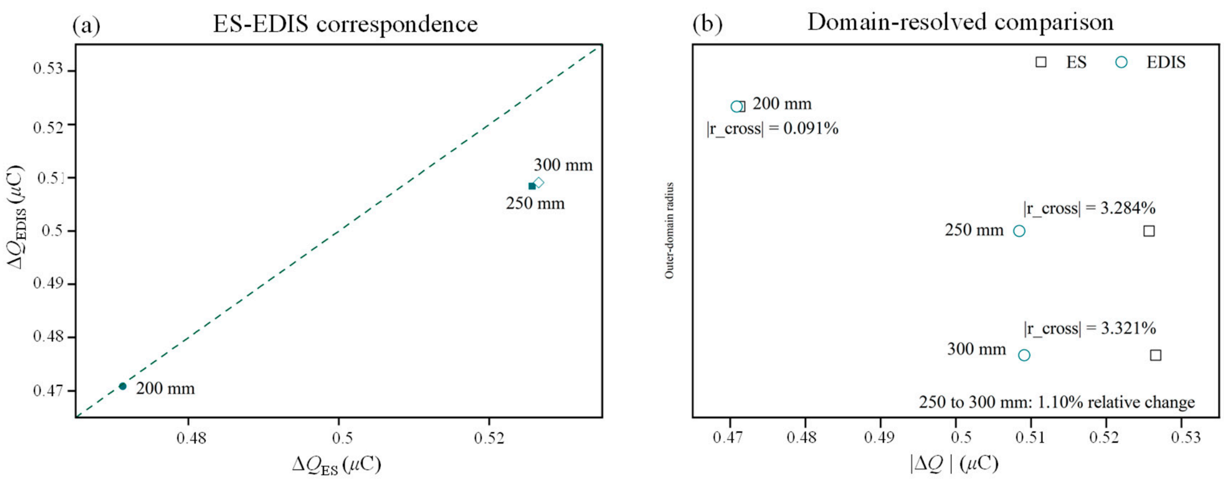

Figure 4. Outer-domain dependence of the 15 kV grounded-boundary integrated response: (**a**) correspondence between $|\Delta Q_{EDIS}|$ and $|\Delta Q_{ES}|$ for outer-air radii of 200, 250, and 300 mm, with the dashed line indicating the 1:1 relation; (**b**) $|\Delta Q_{ES}|$, $|\Delta Q_{EDIS}|$, and the corresponding $|r_{cross}|$ at each outer radius; $\Delta Q = Q(\theta = +3) - Q(\theta = -3)$. Square and circle markers denote ES and EDIS results, respectively.

As shown in Figure 4a, the 200 mm model yields $|\Delta Q_{ES}|$ and $|\Delta Q_{EDIS}|$ of approximately 0.4713 and 0.4708 μC, respectively. When the outer-air radius is increased to 250 mm, the corresponding values rise to approximately 0.5257 and 0.5084 μC; at 300 mm, they are approximately 0.5266 and 0.5091 μC. Thus, ES and EDIS remain on comparable conductor-integrated scales within the same computational domain, but the 200 mm outer-air domain does not reproduce the global boundary-integral values obtained with the enlarged domains.

In Figure 4b, $|r_{cross}|$ is approximately 0.091%, 3.28%, and 3.32% for outer-air radii of 200, 250, and 300 mm, respectively. Increasing the radius from 250 to 300 mm changes $|\Delta Q_{ES}|$ and $|\Delta Q_{EDIS}|$ by only approximately 0.165% and 0.127%, respectively, while the relative change in $|r_{cross}|$ is approximately 1.10%. Compared with the change from 200 to 250 mm, the sensitivity of the conductor-integrated quantities to the outer-domain size is markedly reduced between 250 and 300 mm.

On the basis of this comparison, the 300 mm outer-air domain is used as the reference for subsequent quantitative discussion of conductor-integrated common-ground quantities. In this reference domain, the windowed charge change differs by approximately 3.3% between EDIS and ES, indicating a few-percent-level modification of the global conductor response when charged-particle transport and space-charge feedback are included. This cross-model difference describes the change from ES to EDIS under an identical geometry and integration definition; it is not equivalent to the conductive-current fraction in the experimental terminal current.

3.4. Sensitivity of the History-State Effect to Reset Timing

Figure 5 quantifies the sensitivity of the local H/R state difference to reset-hold time at 15 kV. For reset-hold settings of 0, 1τ, and 2τ, the representative near-tip electron number densities in H are 1.1725×10^9, 1.1715×10^9, and 1.1746×10^9 m^{-3}, respectively; the corresponding values in R are 1.0127×10^9, 1.0142×10^9, and 1.0169×10^9 m^{-3}.

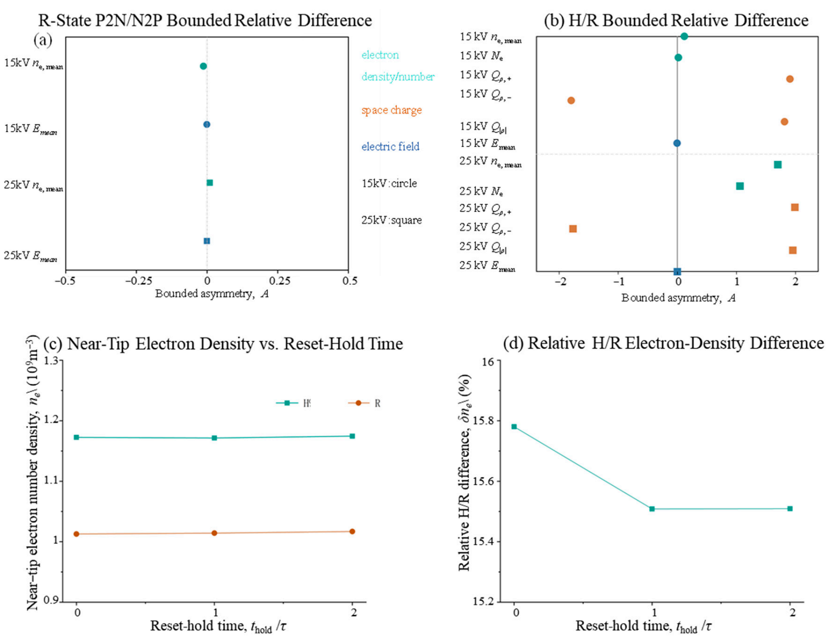

Figure 5. Quantitative comparison of reversal-path and history-state effects and their sensitivity to reset-hold time at 15 kV: (**a**) signed bounded relative differences between the P2N-R and N2P-R states; (**b**) signed bounded relative differences between the H and R states; (**c**) near-tip electron number density for the H and R states at reset-hold times of 0, 1τ, and 2τ; and (**d**) the corresponding relative H/R difference in near-tip electron number density. Teal, orange, and blue denote electron, space-charge, and electric-field quantities, respectively; circles and squares denote the 15 and 25 kV cases.

Using the same definition, the relative H/R differences in near-tip electron number density are 15.8%, 15.5%, and 15.5% for the three reset-hold times. Thus, over the tested 0–2τ range, changing the reset-hold time neither reverses the ordering H > R nor alters the conclusion that H/R difference persists across the tested reset-time settings; the variation in the relative difference is a sub-percentage point.

By contrast, the conductor-integrated common-ground quantities for H and R are almost coincident under these conditions. Their direct difference lies on the numerical scale of 10^{-21}–10^{-20} C. We therefore interpret only that the global H/R common-ground integrated responses are indistinguishable at the present numerical resolution. The quantitative history-state sensitivity statement is restricted to the completed 0–2τ reset-time range.

3.5. Grounded-Boundary Response over the 5–15 kV Voltage Range

To examine the voltage trend over the experimental range, the EDIS common-ground boundary-integrated quantity of the H state was additionally extracted at 5 and 10 kV using the same fixed-domain definition as that used in the 15 kV baseline case. The resulting $|Q_{EDIS}|$ values at 5, 10, and 15 kV are approximately 1.57×10^{-7}, 3.15×10^{-7}, and 4.72×10^{-7} C, respectively.

Over this voltage range, the conductor-integrated quantity increases approximately in proportion to the applied-voltage magnitude, indicating that the dominant scale of the global boundary response is controlled primarily by the applied-voltage excursion. This 5–15 kV comparison is used to assess voltage scaling, whereas the matched-domain analysis at 200/250/300 mm in Section 3.3 evaluates outer-domain sensitivity for the representative 15 kV condition; the two numerical comparisons therefore serve different purposes.

4. Experimental Measurements and Statistical Analysis

4.1. Experimental Platform

The platform shown in Figure 6 comprises positive and negative DC high-voltage supplies, a polarity-reversal switch, a current-limiting protective resistor, the needle–plane electrode assembly, a high-voltage divider, a Rogowski coil, a digital storage oscilloscope, and a computer. The needle electrode was connected directly to the lower plate through a metallic conductive joint without an intentional insulating gap; both parts were connected to the same grounding conductor, around which the Rogowski coil was installed. The upper plate was connected to the polarity-reversal source through the protective resistor.

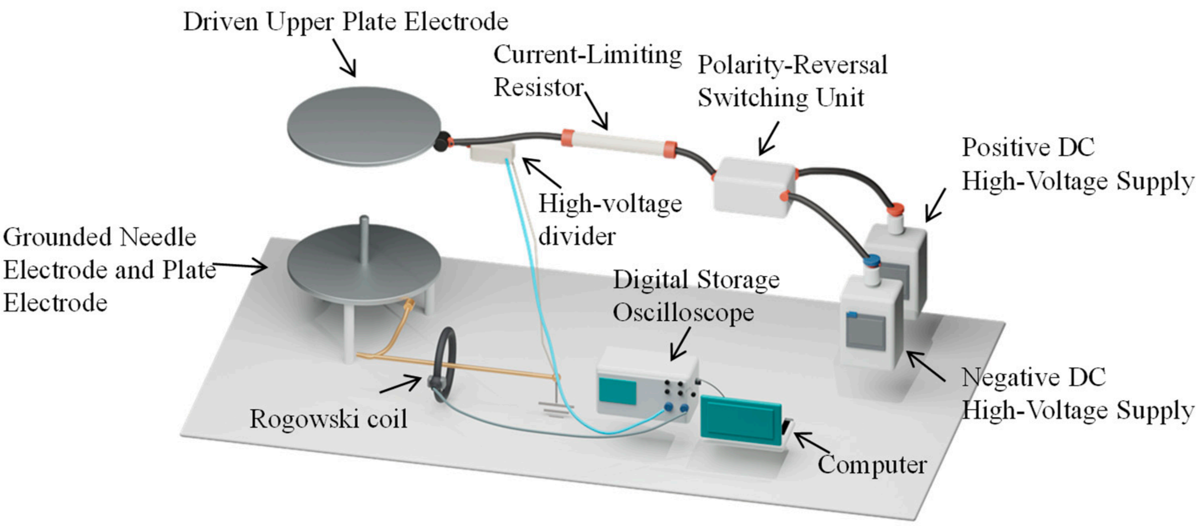

Figure 6. Experimental platform and synchronized measurement system for polarity reversal in the needle–plane air gap.

The high-voltage divider recorded the actual upper-plate voltage on CH1, while the Rogowski coil recorded the transient current in the common grounding conductor on CH2. The latter is therefore a terminal current through the complete common-ground return path rather than a direct measurement of the charged-particle flux at the needle tip. The numerical integration boundary Γ_g was defined using the same needle-plus-lower-plate conductor set.

P2N and N2P reversals were performed at 5, 10, and 15 kV, with 20 repetitions for each combination. The voltage changed from $+V_m$ to $-V_m$ or from $-V_m$ to $+V_m$, respectively, within approximately 3 ms. The fixed time window, peak extraction, zero-crossing determination, and FWHM calculation rules were identical for all 120 events.

4.2. Representative Voltage and Current Waveforms for P2N and N2P Reversals

Figure 7 presents the synchronized voltage and corrected common-ground-current waveforms for P2N and N2P reversals at 10 kV. Figure 7a,b show continuous and monotonic voltage reversal for both directions, with comparable slew rates near the zero crossing and similar overall transition times. No pronounced voltage overshoot or zero-voltage dwell is observed, providing comparable applied-voltage conditions for the current comparison.

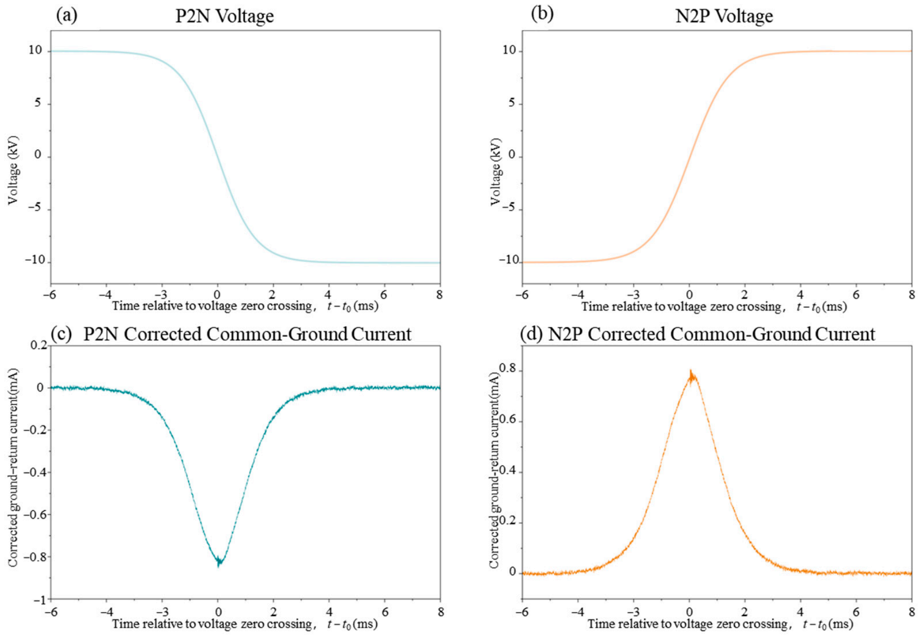

Figure 7. Synchronized voltage and corrected common-ground current for representative 10 kV polarity reversals: (**a**) P2N voltage; (**b**) N2P voltage; (**c**) P2N current; and (**d**) N2P current. All traces are referenced to the zero crossing of the measured voltage.

The two representative waveforms in Figure 7 are approximately mirrored in sign and overall main-pulse morphology. The P2N example has a slightly larger absolute peak and an earlier peak position, whereas the N2P example exhibits a broader trailing edge. A single representative event, however, cannot establish whether these differences constitute a reproducible direction effect. Figure 7 is therefore used to illustrate the typical synchronized voltage–current morphology for the two reversal directions, while in Section 4.3, group-level P2N/N2P differences are evaluated from all repeated events.

4.3. Effects of Voltage Magnitude and Reversal Direction on Transient Features

Figure 8 summarizes all 120 P2N/N2P events at 5, 10, and 15 kV, together with group means and 95% confidence intervals. Both the absolute peak current and the fixed-window absolute integral increase markedly with voltage magnitude, showing that voltage level is a primary determinant of the terminal-transient amplitude.

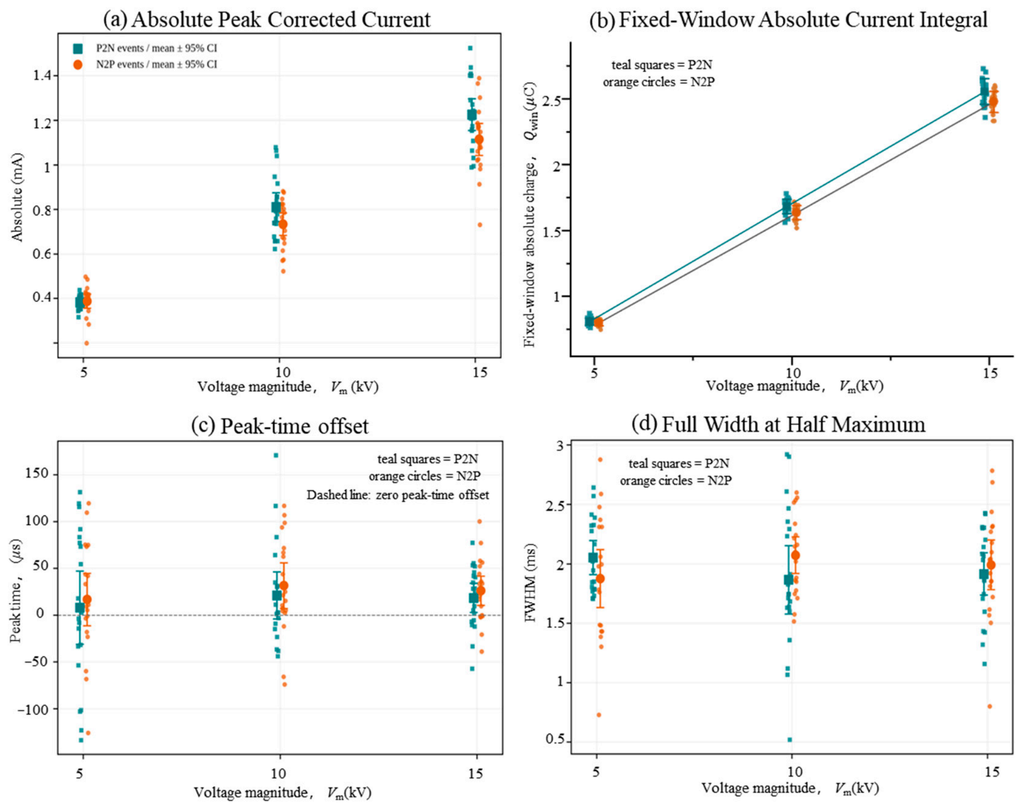

Figure 8. All-event statistical distributions of common-ground-current descriptors for P2N and N2P at 5, 10, and 15 kV: (**a**) absolute peak corrected current; (**b**) fixed-window absolute charge; (**c**) peak-time offset; and (**d**) FWHM. Small symbols denote individual events, and large symbols/error bars denote group means and 95% confidence intervals.

In Figure 8a, the mean peak currents show some offset between reversal directions; however, after Holm correction across the predefined P2N/N2P comparisons, the peak-current direction difference does not remain statistically significant at 5, 10, or 15 kV. The directional difference in peak magnitude is therefore treated as a descriptive trend rather than a general statistically supported effect.

In Figure 8b, Q_{win} increases with voltage excursion. At 15 kV, the mean fixed-window absolute integrals are approximately 2.807 μC for P2N and 2.646 μC for N2P; this difference remains statistically supported after Holm correction (adjusted p = 0.000601, Hedges g = 1.419, 95% bootstrap CI = 0.830–2.260). By contrast, the direction differences at 5 and 10 kV do not reach the same level of evidence after multiplicity correction.

Figures 8c and 8d show the peak-time offset and FWHM, respectively. Both descriptors exhibit direction-related offsets in their group means, but the P2N/N2P comparisons do not remain statistically significant after multiplicity correction. Peak-time offset is particularly sensitive to the determination of the voltage zero crossing, inter-channel delay, and local high-frequency perturbations, and consequently shows greater within-group dispersion than do the peak magnitude and Q_{win}.

Figure 8 therefore supports two levels of experimental inference: the peak magnitude and Q_{win} show robust amplitude scaling with voltage, while among the tested direction-sensitive terminal quantities, the 15 kV fixed-window absolute integral has the strongest statistical support. Directional differences in peak magnitude, peak timing, and FWHM are retained only as descriptive waveform features. The corresponding group-level P2N/N2P statistical comparisons are summarized in Table 3.

Table 3. P2N/N2P statistical comparisons for 20 repeated events per condition; group values are means [95% CI].

Voltage	Metric	P2N	N2P	Holm p	Hedges g
5 kV	Peak current (mA)	0.383 [0.368, 0.398]	0.389 [0.357, 0.420]	1.000	−0.10
5 kV	Peak-time offset (μs)	8.075 [−31.062, 47.212]	16.825 [−11.150, 44.800]	1.000	−0.12
5 kV	FWHM (ms)	2.055 [1.911, 2.198]	1.878 [1.634, 2.122]	1.000	0.40
5 kV	Q_{win} (μC)	0.922 [0.907, 0.937]	0.892 [0.871, 0.913]	0.218	0.76
10 kV	Peak current (mA)	0.811 [0.746, 0.876]	0.734 [0.684, 0.784]	0.464	0.61
10 kV	Peak-time offset (μs)	21.088 [−4.005, 46.180]	31.700 [7.325, 56.075]	1.000	−0.20
10 kV	FWHM (ms)	1.867 [1.579, 2.155]	2.073 [1.919, 2.228]	1.000	−0.41
10 kV	Q_{win} (μC)	1.857 [1.795, 1.920]	1.773 [1.716, 1.830]	0.394	0.65
15 kV	Peak current (mA)	1.226 [1.155, 1.297]	1.115 [1.043, 1.187]	0.276	0.71
15 kV	Peak-time offset (μs)	18.550 [2.844, 34.256]	26.263 [10.699, 41.826]	1.000	−0.23
15 kV	FWHM (ms)	1.916 [1.738, 2.094]	1.993 [1.784, 2.201]	1.000	−0.18
15 kV	Q_{win} (μC)	2.807 [2.752, 2.862]	2.646 [2.597, 2.695]	0.000601	1.42

4.4. Repeatability of the P2N Common-Ground Current

Figure 9 shows 20 repeated P2N measurements at each of the three voltage magnitudes. The left column retains all individual waveforms and the mean, while the right column shows the mean and the standard-deviation band. Each waveform is aligned to the zero crossing of its own measured voltage.

At 5 kV, all 20 events form a single negative peak of approximately 0.4 mA, with consistent pre-peak rise, peak time, and post-peak decay. Outside the reversal interval, the current returns stably to the zero baseline without a persistent DC offset.

At 10 kV, the absolute peak increases to approximately 0.8 mA, while the 20 repeated tests retain a similar waveform structure. The absolute standard deviation near the peak increases with the signal amplitude, but the ratio to the mean peak does not increase appreciably, indicating that the larger current does not degrade waveform repeatability.

At 15 kV, the mean peak reaches 1.2–1.3 mA. The pre-peak and post-peak curves continue to overlap closely, and no systematic shift of the main peak is observed. The standard deviation is concentrated on the two sides of the peak where the waveform slope is large, whereas the baseline and decay tail exhibit less scatter.

The pointwise standard deviation around the principal pulse reflects both amplitude fluctuations and peak-time fluctuations. When the peak times of individual events differ slightly, the rising and falling edges correspond to different current values at the same sampling instant, broadening the standard-deviation band in the high-slope regions. The band in Figure 9 therefore reflects both amplitude dispersion and temporal dispersion among the repeated waveforms.

At all three voltage magnitudes, the P2N current retains a stable single-peak structure and a similar normalized temporal profile. The repeated measurements therefore provide a consistent within-group waveform basis for event-level feature extraction and subsequent inter-group statistical comparison.

4.5. Voltage-Driven Scaling and Robustness of the Capacitive Baseline

Figure 10 compares the temporal and amplitude-scaling relationships between the common-ground current and the polarity-reversal voltage change. The representative normalized waveform shows a strong correspondence between the main I_{corr} pulse and signed dV/dt in both peak position and principal temporal extent. Across all events, the absolute peak current increases approximately with max|dV/dt|, whereas the fixed-window absolute integral Q_{win} increases with the voltage excursion ΔV. Together, these scaling relationships indicate that the dominant amplitude scale of the common-ground transient is closely associated with the applied-voltage variation and the effective capacitance of the system.

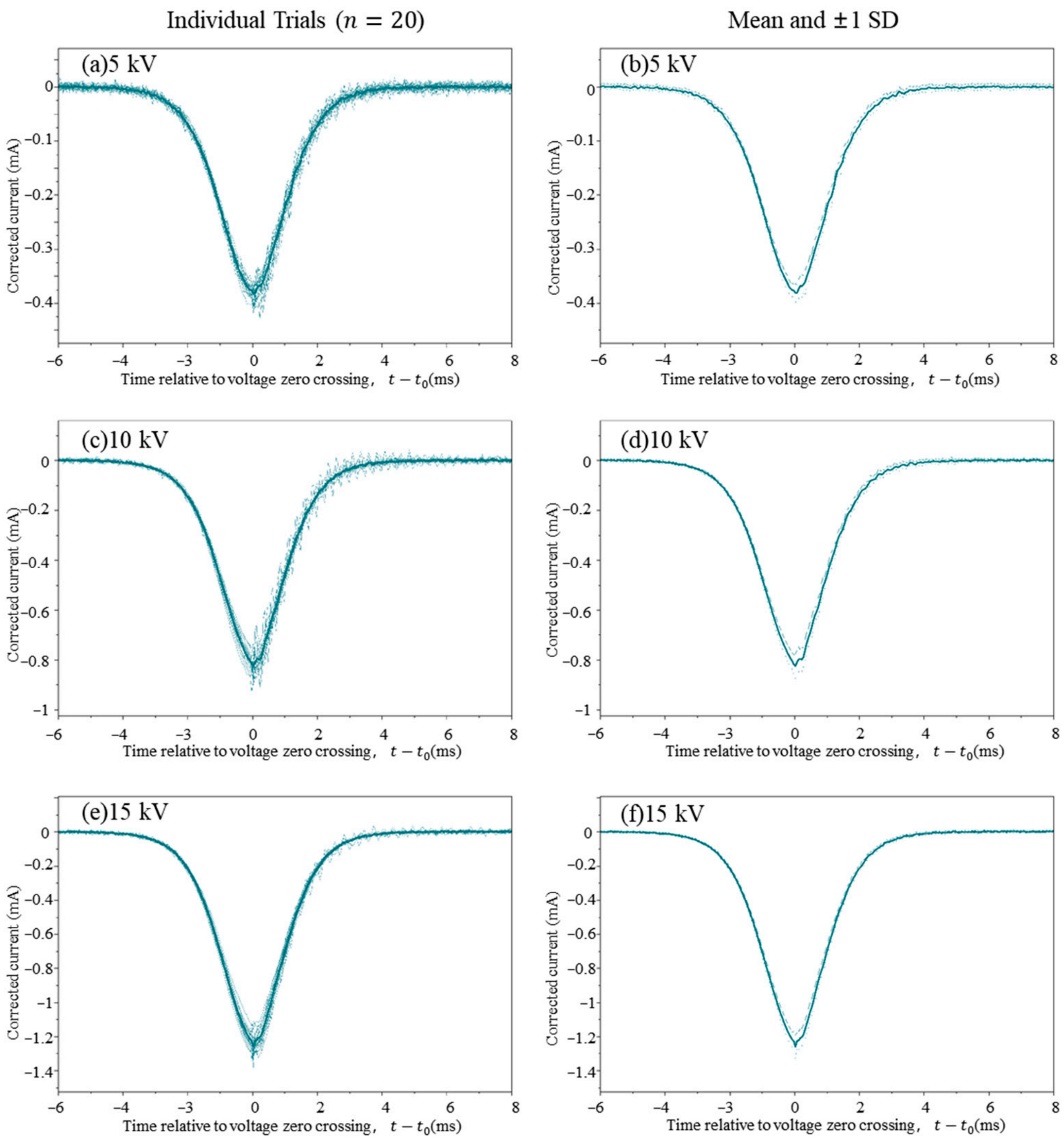

Figure 9. Repeatability of the P2N common-ground current at 5, 10, and 15 kV: (**a**,**c**,**e**) 20 individual measured waveforms and their mean; and (**b**,**d**,**f**) the mean waveform and standard-deviation band. Thin curves represent individual measurements, the solid curve represents the mean, and the shaded band represents ±1 standard deviation.

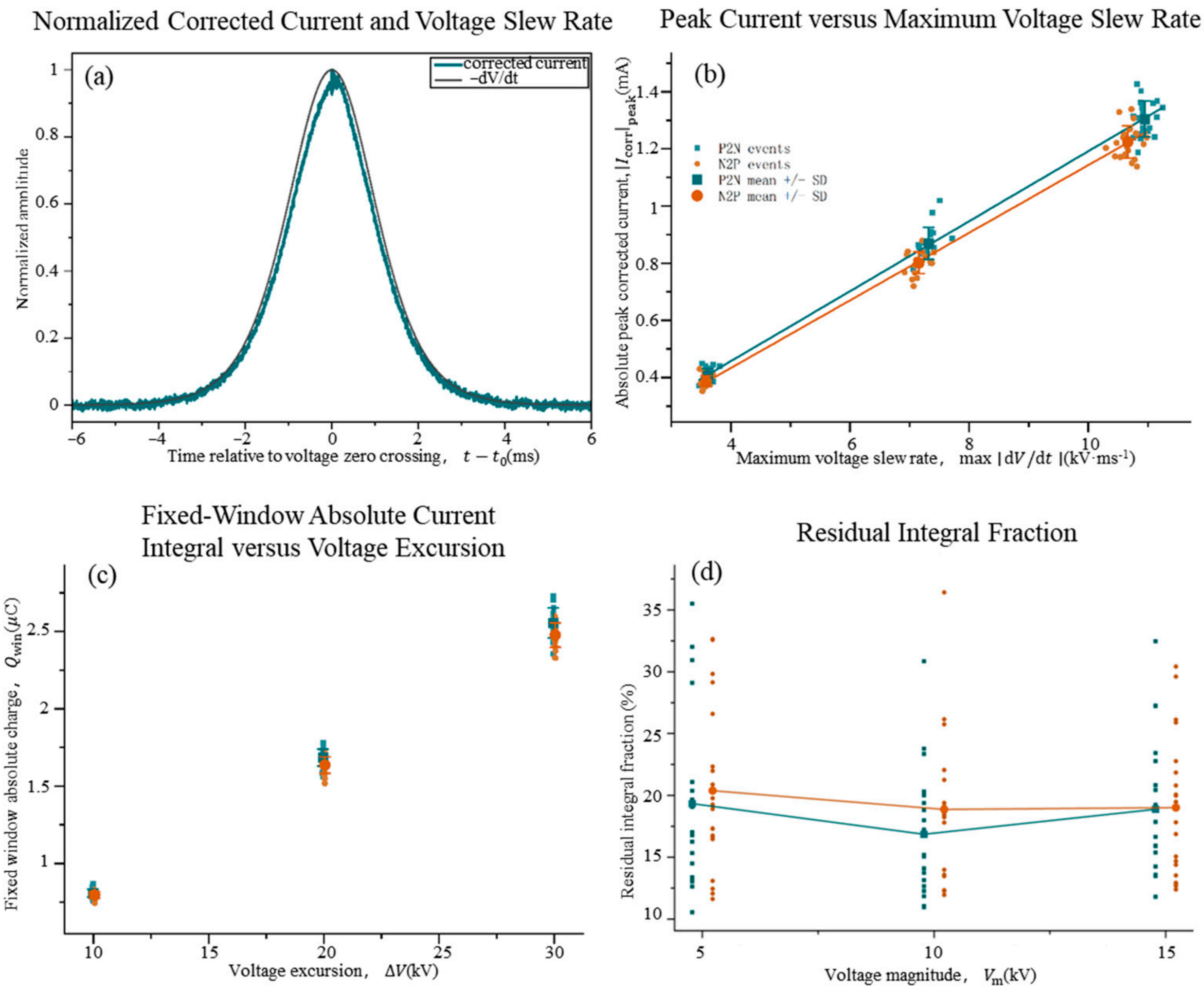

Figure 10. Voltage-driven scaling characteristics of the common-ground transient response: (**a**) representative normalized corrected current and voltage-slew reference; (**b**) absolute peak current versus maximum |dV/dt|; (**c**) fixed-window absolute charge versus voltage excursion; and (**d**) event-level residual fraction by voltage and reversal direction.

To avoid conclusions based on a selected representative trace, Figure 11a evaluates the Pearson correlation between the corrected common-ground current and signed dV/dt for each of the 120 events over the fixed interval from −3 to +4 ms. The median is 0.989253, the empirical 95% interval is 0.968014–0.995283, and the full range is 0.962748–0.995386. These results demonstrate a reproducible event-level temporal correspondence between the voltage-slew waveform and the common-ground current; the high correlation itself is not used to uniquely identify the microscopic composition of the current.

Figure 11b shows the fitted C_{app} distributions. At 15 kV, the median C_{app} values are approximately 92.85 pF for P2N and 88.10 pF for N2P, substantially larger than the approximately 17.55 pF structural capacitance of the finite numerical geometry. The experimental C_{app} includes the high-voltage divider, polarity-reversal switching unit, cables, connecting conductors, sensor, and other stray capacitances and is therefore treated as an apparent parameter of the complete measurement system rather than as the finite-element geometrical capacitance itself.

Figure 11c shows a residual median of 17.86% with the same-event baseline; the median increases to 19.30% with the leave-one-out baseline and is 19.13% with the group-level baseline. The empirical 95% intervals for the same-event and LOO constructions are 11.60–32.57% and 12.39–34.63%, respectively. These results show that the residual response is not eliminated by removing the same-event fit, although its magnitude is sensitive to the baseline construction.

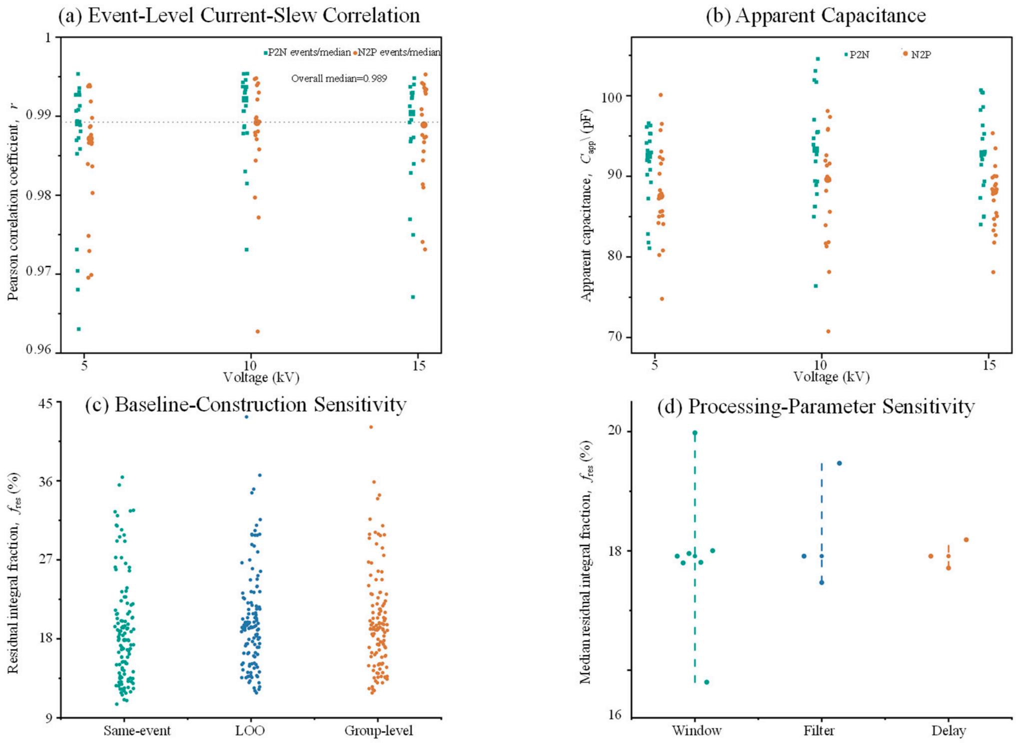

Figure 11. Robustness of the fitted capacitive baseline and residual analysis: (**a**) event-level Pearson correlation between corrected common-ground current and signed dV/dt; (**b**) apparent-capacitance distributions; (**c**) same-event, leave-one-out, and group-level baseline sensitivity; and (**d**) ranges of median residual values under fitting/integration-window, filter, and channel-delay perturbations.

Figure 11d further examines perturbations of the fitting/integration window, filter window, and channel-delay treatment. The corresponding residual medians span approximately 15.80–19.98%, 17.47–19.47%, and 17.71–18.19%, respectively. Accordingly, f_{res} is defined here as a processing-dependent non-baseline contribution relative to the fitted single-capacitance baseline. It may contain contributions associated with charged-particle/space-charge motion, together with measurement-chain transfer, switching coupling, channel delay, filtering, and inadequacy of the single-capacitance model and therefore, cannot be interpreted directly as a pure conduction-current fraction.

Taken together, Figures 10 and 11 show that the common-ground terminal response under the present conditions has a pronounced voltage-slew/capacitance-controlled dominant scale, while retaining a nonzero non-baseline component with finite processing sensitivity. The experimental residual and the numerical ES-EDIS cross-model difference are defined differently and are therefore used to describe deviations at different observational levels rather than numerically equated as the same physical component.

5. Discussion

5.1. Difference Between Local Particle States and the Grounded-Boundary Integrated Response

The numerical and experimental results jointly reveal a pronounced dependence on observational scale during polarity reversal. Figures 2, 3 and 5 show that the reversal path and the pre-reversal particle history modify the electron and space-charge distributions near the needle tip; in particular, the H/R reset-time comparison retains an approximately 15–16% difference in representative near-tip electron state over 0–2τ. By contrast, the outer-domain-checked conductor-integrated ES–EDIS difference for the representative 15 kV case in Figure 4 is approximately 3.3%, while the complete H/R common-ground integrated responses are essentially coincident at the present numerical resolution.

This contrast arises from the different spatial definitions of the two observables. Electron density and space charge characterize the local particle state in the high-field region near the needle tip and are highly sensitive to ionization, attachment, recombination, and drift. Q_{ground}, by contrast, is the integral of electric-displacement flux over the entire needle and lower-plate surfaces. Contributions induced by adjacent positive and negative space-charge regions near the tip may also partially cancel when integrated over the complete grounded conductor. Consequently, no simple proportional mapping exists between the local charged-particle state and the conductor-integrated response.

The experimental results show a consistent hierarchy. The main common-ground-current pulse increases with voltage slew rate and voltage excursion, while a central non-baseline level of approximately 18–19% remains after subtraction of the fitted capacitive baseline. This experimental residual and the numerical cross-model difference have different definitions and cannot be compared as percentages; rather, both support treating local particle variation and the externally measured complete-conductor response as observables at different scales.

5.2. Local Space-Charge Memory and Direction-Dependent Common-Ground-Current Features

During polarity reversal, the applied electric field changes direction on the τ_{rev} time scale, whereas the electron, positive-ion, and negative-ion distributions established before reversal do not vanish synchronously at the voltage zero crossing. According to Equation (7), the local net space charge depends on $n_p - n_e - n_n$ and, through Poisson coupling, modifies the near-tip electric field while the different charged species continue to evolve through their respective drift, diffusion, and reaction processes.

Electron transport and attachment occur on different characteristic time scales from positive- and negative-ion migration and recombination [37]. The residual charge configuration from the preceding stage can therefore produce different degrees of field screening or field reinforcement as the post-reversal field is re-established. Consequently, even at the same instantaneous $|V|$, P2N and N2P are not required to produce mirror-symmetric electron and space-charge distributions. The near-tip particle reorganization shown in Figures 2 and 3, together with the H/R sensitivity in Figure 5, provides numerical evidence for this history-dependent process [18–22,29,32–34].

A second scale transition occurs between the local state and the terminal current. Contributions from local positive and negative space-charge regions to the electric-displacement flux over the complete Γ_g can be partially canceled, while the experimental terminal response also contains the system capacitance and measurement-chain contributions. Local direction/history differences can therefore produce direction-sensitive terminal deviations without being transferred in the same relative proportion to current peak, peak time, or FWHM.

The all-event statistics further delimit the evidential strength of this mechanistic interpretation. P2N/N2P differences in peak magnitude, peak-time offset, and FWHM are retained only as descriptive trends after multiplicity correction, whereas the 15 kV fixed-window absolute integral is the direction-sensitive terminal quantity with the strongest statistical support. We therefore interpret the P2N/N2P mechanism as a physically consistent link between path/history-dependent near-tip charge reorganization and direction-sensitive terminal response, without assigning any single peak or pulse-width difference uniquely to one microscopic process.

5.3. Distinct Roles of Reversal Direction, History State, and Voltage Magnitude

Reversal direction, particle history, and voltage magnitude represent three distinct control dimensions. The P2N/N2P comparison changes the reversal direction, the sign of dV/dt, and the voltage history by which a given observation state is reached. The H/R comparison changes the initial charged-particle state while keeping the subsequent voltage function unchanged. Voltage magnitude, in turn, changes both the near-tip high-field strength and the capacitive response scale of the complete structure.

The P2N–R/N2P–R comparison shows that the instantaneous voltage alone does not uniquely determine the local morphology of the near-tip electron and space-charge distributions. The H/R comparison further shows that the charged-particle state inherited from the preceding stage can modify the subsequent near-tip particle organization, while its effect on the conductor-integrated quantity of the complete common-ground assembly is substantially weaker than that of the local-state difference.

Increasing voltage magnitude simultaneously raises the local high-field intensity and the experimental terminal-transient amplitude. The original 15/25 kV numerical cases were used to compare local particle states at higher field strengths; the additional 5/10/15 kV fixed-domain results show that the common-ground integrated quantity increases approximately in proportion to voltage magnitude, providing direct overlap with the experimental 5–15 kV range. The shared 15 kV condition is used for the more detailed numerical–experimental comparison below, whereas 25 kV is retained only as a higher-field local-state condition.

Within the combined 5–25 kV range and weak-discharge conditions investigated here, the numerical results do not exhibit a continuous high-density channel bridging the 50 mm gap, and the experimental waveforms do not show a sustained conduction plateau independent of the reversal edge. The present discussion therefore concerns a non-bridging polarity-reversal transient rather than streamer bridging or breakdown.

5.4. Correspondence Between Numerical and Experimental Results

The numerical model and the experiment provide complementary evidence at different observational levels. EDIS resolves internal quantities such as electron number density, space charge, electric field, and the common-ground boundary-integrated response, whereas the experiment records the upper-plate voltage and the current of the complete common-ground return path synchronously. Numerical–experimental correspondence is therefore established first through voltage dependence and conductor-level observables rather than by equating model-internal particle densities with the Rogowski-coil current.

Under the common 15 kV condition, numerical–experimental correspondence is quantified using normalized conductor-level waveform descriptors and timing parameters rather than by relying on a separate waveform-overlay figure. The structural capacitance obtained from the 300 mm numerical geometry is used to construct the ES conductor reference, and the same descriptors are calculated against the experimental group-mean waveform on the common dimensionless time coordinate θ. For P2N/N2P, the normalized waveform correlations are 0.99937 and 0.99915, the NRMSE values are 0.03075 and 0.02455, the normalized peak offsets are 0.0158 and 0.0313, and the FWHM ratios are 0.925 and 0.959, respectively. These quantities are summarized in Table 4 for direct inspection under the common 15 kV condition.

The numerical structural capacitance is approximately 17.55 pF, whereas the median experimental C_{app} values are approximately 92.85 pF for P2N and 88.10 pF for N2P. This difference is consistent with the different electrical boundaries of the model and experiment: the finite-element model contains only the finite electrodes and air domain, whereas the experimental circuit also includes connecting conductors, the voltage divider, the polarity-reversal switching unit, cables, sensors, and their associated stray capacitances. We therefore compare normalized waveform/timing quantities and do not impose an artificial amplitude scaling to force the experimental mA peaks to coincide with the numerical current.

Table 4. Quantitative 15 kV numerical–experimental comparison using normalized conductor-level observables.

Direction	n	r_{shape}	NRMSE	$\Delta\theta_{\mathrm{peak}}$	FWHM Ratio	$C_{\mathrm{num}}/Capp$ (pF)
P2N	20	0.99937	0.03075	0.0158	0.925	17.55/92.85
N2P	20	0.99915	0.02455	0.0313	0.959	17.55/88.10

This comparison evaluates the shape and timing correspondence of the conductor-level response; it does not constitute direct experimental validation of the model-internal near-tip n_e or ρ. The experiment did not include emission spectroscopy, absorption spectroscopy, or another independent optical diagnostic capable of quantitatively retrieving the near-tip electron density. The particle states in Figures 2, 3 and 5 therefore remain model predictions. The synchronized external voltage–current measurements test the hierarchy of terminal responses rather than back-validate the absolute value of a local numerical field.

The r_{shape} values in Table 4 compare the 15 kV group-mean normalized waveform with the ES conductor reference, whereas Figure 11a calculates an event-level Pearson correlation between corrected common-ground current and signed dV/dt separately for each of the 120 experimental events. The compared quantities and statistical levels are different: the former measures numerical–experimental shape correspondence under the common condition, whereas the latter characterizes the waveform-level capacitive relation across experimental events. The two sets of correlation coefficients should therefore not be interpreted as the same statistic.

5.5. Applied Implications and Validity Range

For weak-discharge monitoring under polarity-switching conditions, the present results show that a large raw common-ground-current peak cannot be equated directly with stronger local discharge. The synchronized voltage can first be used to establish a C_{eff} dV/dt type terminal baseline, after which the fixed-window integral and repeatable deviations from that baseline can be evaluated. This procedure helps distinguish the main pulse dominated by the switching-capacitive background from weaker non-baseline responses. The interpretation is consistent with measurements of weak corona currents from grounded rods under thunderstorm background fields, where the distinction between a grounded-terminal signal and the local corona state is likewise important [18,19].

For measurement systems and insulation diagnostics, the approximately 17.55 pF numerical structural capacitance and approximately 88–93 pF experimental C_{eff} values demonstrate that parasitic capacitances associated with the voltage divider, cables, switch, connecting conductors, and sensor chain can substantially alter the terminal-transient amplitude. Measurement topology and stray-capacitance conditions should therefore be controlled before raw currents are compared across different insulation states or devices.

The reversal rate constitutes an independent validity parameter. For the tanh voltage trajectory used here, the maximum voltage slew rate satisfies

$$\left|\frac{\mathrm{d}V}{\mathrm{d}t}\right|_{\max} = \frac{V_{\mathrm{m}}}{\tau_{\mathrm{rev}}} \tag{26}$$

The corresponding first-order capacitive terminal scale can be approximated as

$$I_{\mathrm{D,max}} \approx C_{\mathrm{eff}} \frac{V_m}{\tau_{\mathrm{rev}}} \tag{27}$$

Thus, for fixed V_m and C_eff, reducing τ_rev directly increases the dV/dt-related capacitive transient. At the same time, a faster reversal leaves less time for the charged-particle distribution established before reversal to redistribute. Because drift, attachment, ionization, and recombination have different characteristic time scales, the conduction-to-capacitive balance under microsecond- or nanosecond-scale reversal cannot be extrapolated directly from the present approximately 3 ms data.

Geometrical parameters likewise modify this response hierarchy. A smaller tip radius generally enhances the local electric field and changes ionization conditions, while changing the gap alters the mean field, charged-particle transport distance, and electrode capacitance simultaneously. Discharge paths associated with grounded high-field structures such as wind-turbine receptors also exhibit pronounced geometrical and polarity dependence [20]. In addition, practical voltage reversal in systems such as LCC-HVDC insulation involves the same general issue, i.e., that the pre-reversal space-charge state can influence the post-reversal field [38]; however, the solid dielectric, time scale, and transport mechanisms differ fundamentally from those of the present air-gap model, so this serves only as engineering context for polarity-reversal memory and is not used for quantitative extrapolation. The conclusions of this study are restricted to the driven-upper-plate/common-ground needle–lower-plate topology, nominal 0.5 mm tip radius, 50 mm gap, atmospheric-pressure air, combined 5–25 kV investigation range, approximately 3 ms polarity reversal, and weak/non-bridging conditions. Different tip radii, gaps, high-voltage-needle/grounded-plane topology, microsecond/nanosecond reversal, and strong corona/streamer/leader/arc regimes require independent validation.

6. Conclusions

A two-level numerical framework comprising electrostatic and EDIS models was established for a 50 mm needle–plane air gap under bidirectional polarity reversal, and synchronized voltage/common-ground-current measurements were performed at 5, 10, and 15 kV. The numerical and experimental results support the following conclusions.

(1) At the same instantaneous positive voltage, P2N–R and N2P–R exhibit comparable principal near-tip electric-field structures but path-dependent near-tip electron-density and space-charge distributions. The H/R control further shows that, under the same subsequent voltage function, retaining the pre-reversal charged-particle state produces a stable local history-dependent state; over the 0–2τ reset-time range, the representative near-tip electron quantity retains an H/R difference of approximately 15–16%.

(2) The conductor-integrated common-ground quantity is sensitive to the artificial outer-air domain. The representative 15 kV ES–EDIS differences for outer radii of 200, 250, and 300 mm are approximately 0.091%, 3.28%, and 3.32%, respectively, with markedly improved stability from 250 to 300 mm. Using the 300 mm domain as the reference for conductor-integrated analysis yields a representative cross-model difference of approximately 3.3%. The complete H/R common-ground integrated responses are indistinguishable at the present numerical resolution.

(3) The common-ground current forms a reproducible single main pulse at 5, 10, and 15 kV, with amplitude increasing with voltage magnitude and maximum voltage slew rate. Across all 120 events, the median Pearson correlation between corrected current and signed dV/dt is approximately 0.989, indicating a reproducible temporal correspondence between the main terminal waveform and the voltage-slew process.

(4) The fitted capacitive-baseline analysis yields a nonzero residual response. Residual medians are approximately 17.86%, 19.30%, and 19.13% for the same-event, LOO, and group-level baselines, respectively, with finite but non-negligible sensitivity to the fitting window, filtering, and channel delay. After multiplicity correction, the 15 kV fixed-window absolute integral is the P2N/N2P direction-sensitive terminal quantity with the strongest statistical support; directional differences in peak magnitude, peak timing, and FWHM are retained only as descriptive trends.

(5) Taken together, the local particle state, conductor-integrated quantity, and common-ground current show that polarity reversal can preserve a path/history-dependent charged-particle organization near the needle tip, but this local difference is not transferred in the same relative proportion to the complete common-ground response. Under the present millisecond-scale, weak/non-bridging common-ground conditions, the dominant scale of the terminal transient remains closely associated with the applied-voltage variation and the capacitive response of the system.

Author Contributions: Conceptualization, S.D.; methodology, L.Z.; software, Y.Z.; validation, S.D.; formal analysis, S.D.; investigation, L.Z.; data curation, L.Z.; writing—original draft preparation, K.C.; visualization, I.R.U.; writing—review and editing, N.N.u.K.; resources, H.Z.; funding acquisition, H.Z. All authors have read and agreed to the published version of the manuscript.

Funding: This work was supported by the National Key Research and Development Program of China–Intergovernmental International Scientific and Technological Innovation Cooperation (Grant No. 2025YFE0106900).

Institutional Review Board Statement: Not applicable.

Informed Consent Statement: Not applicable.

Data Availability Statement: The data supporting the findings of this study are available from the corresponding author upon reasonable request.

Conflicts of Interest: The authors declare no conflicts of interest.

References

1. Nijdam, S.; Teunissen, J.; Ebert, U. The physics of streamer discharge phenomena. *Plasma Sources Sci. Technol.* **2020**, *29*, 103001. [CrossRef]
2. Asipuela, A.; Iváncsy, T. Study and numerical simulation of negative and positive corona discharge: A review. *Period. Polytech. Electr. Eng. Comput. Sci.* **2022**, *66*, 294–300. [CrossRef]
3. Ren, X.; Jiang, X.; Yang, G.; Huang, Y.; Wu, J.; Yang, Z. Effect of environmental parameters on streamer discharge in short air gap between rod and plate. *Energies* **2022**, *15*, 817. [CrossRef]
4. Salah, W.S.; Gazeli, O.; Lazarou, C.; Anastassiou, C.; Georghiou, G.E. Investigation of negative corona discharge Trichel pulses for a needle–plane geometry via two numerical 2D axisymmetric models. *AIP Adv.* **2022**, *12*, 105123. [CrossRef]
5. Iqbal, A.; Wozniak, D.; Rahman, M.Z.; Banerjee, S.; Verboncoeur, J.; Zhang, P.; Jiang, C. Influence of discharge polarity on streamer breakdown criterion of ambient air in a non-uniform electric field. *J. Phys. D Appl. Phys.* **2023**, *56*, 035204. [CrossRef]
6. Yin, K.; An, Y.; Hu, Y.; Qu, L.; Liu, X.; Lin, Y.; Su, M.; Yang, M.; Wang, Q.; Sha, X. Experimental study on positive corona discharge characteristics in plane-single/double earthed rods air gaps under negative DC voltage. *Electr. Power Syst. Res.* **2023**, *216*, 109058. [CrossRef]
7. Uckol, H.I.; Ilhan, S. Characterization of DC corona discharge current pulses using high-frequency measurement techniques. *Measurement* **2023**, *218*, 113154. [CrossRef]
8. Dai, Y.; Zhang, Z.; Dong, Z.; Wu, Y.; Deng, J. Research on ultraviolet characteristic parameters of DC-positive polarity corona discharge on conductors. *Appl. Sci.* **2024**, *14*, 3258. [CrossRef]
9. Guo, B.; Ebert, U.; Teunissen, J. 3D modeling of positive streamers in air with inhomogeneous density. *Plasma Sources Sci. Technol.* **2023**, *32*, 095015. [CrossRef]
10. Wang, Z.; Wu, B.; Guo, X.; Zhao, N.; Zhang, H.; Zhao, Y.; Zheng, Y. The development and application of a three-dimensional corona discharge numerical model considering the thunderstorm electric-field polarity-reversal process. *Atmosphere* **2025**, *16*, 612. [CrossRef]

11. Ferreira, N.G.C.; Almeida, P.G.C.; Eivazpour Taher, A.; Naidis, G.V.; Benilov, M.S. Numerical investigation of stability of low-current needle-to-plane negative corona discharges in air. *Plasma Sources Sci. Technol.* **2025**, *34*, 085002. [CrossRef]
12. Zhang, H.; Guo, X.; Wang, Z.; Zhao, Y.; Zheng, Y.; Liu, S. Study on the Characteristics of Positive and Negative Corona Discharge of an Independent Lightning Rod Under Different Background Electric Field Amplitude. *Atmosphere* **2026**, *17*, 428. [CrossRef]
13. Briels, T.M.P.; Kos, J.; Winands, G.J.J.; van Veldhuizen, E.M.; Ebert, U. Positive and negative streamers in ambient air: Measuring diameter, velocity and dissipated energy. *J. Phys. D Appl. Phys.* **2008**, *41*, 234004. [CrossRef]
14. Shafiq, M.; Stewart, B.G.; Hussain, G.A.; Hassan, W.; Choudhary, M.; Palo, I. Design and applications of Rogowski coil sensors for power system measurements: A review. *Measurement* **2022**, *203*, 112014. [CrossRef]
15. Xiao, Y.; Jiao, H.; Huo, F.; Shen, Z. Lightning current measurement method using Rogowski coil based on integral circuit with low-frequency attenuation feedback. *Sensors* **2024**, *24*, 4980. [CrossRef] [PubMed]
16. Morrow, R.; Sato, N. The discharge current induced by the motion of charged particles in time-dependent electric fields: Sato's equation extended. *J. Phys. D Appl. Phys.* **1999**, *32*, L20–L22. [CrossRef]
17. Pan, C.; Wu, K.; Du, Y.; Tang, J. Comparison of Sato's equation and Pedersen's theory to obtain gas discharge current. *IEEE Trans. Dielectr. Electr. Insul.* **2016**, *23*, 1690–1698. [CrossRef]
18. Arcanjo, M.A.; Montanyà, J.; Urbani, M.; Lorenzo, V.; Pineda, N. Observations of corona point discharges from grounded rods under thunderstorms. *Atmos. Res.* **2021**, *247*, 105238. [CrossRef]
19. Arcanjo, M.A.; Montanyà, J.; Urbani, M.; Lorenzo, V. Measuring low-current discharges from grounded rods under high background electric fields. *Electr. Power Syst. Res.* **2023**, *217*, 109139. [CrossRef]
20. Guo, Z.; Li, Q.; Ma, Y.; Ren, H.; Fang, Z.; Chen, C.; Siew, W.H. Experimental study on lightning attachment manner to wind turbine blades with lightning protection system. *IEEE Trans. Plasma Sci.* **2019**, *47*, 635–646. [CrossRef]
21. Zhao, Z.; Li, J. Repetitively pulsed gas discharges: Memory effect and discharge mode transition. *High Volt.* **2020**, *5*, 569–582. [CrossRef]
22. Fan, R.; Wang, Y.; Zhang, X.; Tu, Z.; Zhang, J. The regulation of memory effect and its influence on discharge properties of a dielectric barrier discharge driven by bipolar pulse at atmospheric-pressure nitrogen. *Plasma Sci. Technol.* **2021**, *23*, 105401. [CrossRef]
23. Viegas, P.; Slikboer, E.; Bonaventura, Z.; Garcia-Caurel, E.; Guaitella, O.; Sobota, A.; Bourdon, A. Quantification of surface charging memory effect in ionization wave dynamics. *Sci. Rep.* **2022**, *12*, 1181. [CrossRef] [PubMed]
24. Malla, H.; Martinez, A.; Ebert, U.; Teunissen, J. Double-pulse streamer simulations for varying interpulse times in air. *Plasma Sources Sci. Technol.* **2023**, *32*, 095006. [CrossRef]
25. Peng, Y.; Chen, X.; Wen, X.; Lan, L.; He, W.; Liu, Y.; Zhan, H. Burst pulses for positive corona discharge in an air atmosphere: A simulation study. *IEEE Trans. Plasma Sci.* **2021**, *49*, 1079–1087. [CrossRef]
26. Li, X.; Dijcks, S.; Nijdam, S.; Sun, A.; Ebert, U.; Teunissen, J. Comparing simulations and experiments of positive streamers in air: Steps toward model validation. *Plasma Sources Sci. Technol.* **2021**, *30*, 095002. [CrossRef]
27. Wang, Z.; Sun, A.; Teunissen, J. A comparison of particle and fluid models for positive streamer discharges in air. *Plasma Sources Sci. Technol.* **2022**, *31*, 015012. [CrossRef]
28. Bagheri, B.; Teunissen, J.; Ebert, U.M.; Becker, M.M.; Chen, S.; Ducasse, O.; Eichwald, O.; Loffhagen, D.; Luque, A.; Mihailova, D.; et al. Comparison of six simulation codes for positive streamers in air. *Plasma Sources Sci. Technol.* **2018**, *27*, 095002. [CrossRef]
29. Teunissen, J.; Ebert, U. Simulating streamer discharges in 3D with the parallel adaptive Afivo framework. *J. Phys. D Appl. Phys.* **2017**, *50*, 474001. [CrossRef]
30. Guo, B.; Malla, H.; Malagón-Romero, A.; Teunissen, J. Positive streamer discharge simulations in humid air: Uncertainty in input data and sensitivity analysis. *Plasma Sources Sci. Technol.* **2025**, *34*, 035012. [CrossRef]
31. COMSOL AB. *Electric Discharge Module User's Guide, COMSOL Multiphysics® Version 6.4*; COMSOL AB: Stockholm, Sweden, 2025.
32. Bourdon, A.; Pasko, V.P.; Liu, N.Y.; Célestin, S.; Ségur, P.; Marode, E. Efficient models for photoionization produced by non-thermal gas discharges in air based on radiative transfer and the Helmholtz equations. *Plasma Sources Sci. Technol.* **2007**, *16*, 656–678. [CrossRef]
33. Luque, A.; Ebert, U.; Montijn, C.; Hundsdorfer, W. Photoionization in negative streamers: Fast computations and two propagation modes. *Appl. Phys. Lett.* **2007**, *90*, 081501. [CrossRef]
34. Nijdam, S.; van de Wetering, F.M.J.H.; Blanc, R.; van Veldhuizen, E.M.; Ebert, U. Probing photo-ionization: Experiments on positive streamers in pure gases and mixtures. *J. Phys. D Appl. Phys.* **2010**, *43*, 145204. [CrossRef]
35. Pancheshnyi, S. Photoionization produced by low-current discharges in O_2, air, N_2 and CO_2. *Plasma Sources Sci. Technol.* **2015**, *24*, 015023. [CrossRef]
36. Wei, Z.; Komuro, A.; Ono, R. The influence of individual evaluation of electron-impact ionization, attachment, and photoionization rates on positive streamer propagation. *Plasma Process. Polym.* **2024**, *21*, e2300113. [CrossRef]

https://doi.org/10.3390/app16178536

37. Fushimi, K.; Shirai, N.; Sasaki, K. Detection of negative ions in streamer discharge in air by transient cavity ringdown spectroscopy. *Plasma Sources Sci. Technol.* **2024**, *33*, 02LT01. [CrossRef]
38. Li, Z.; Zheng, Z.; Wu, Y.; Du, B. Space Charge and Electric Field Dependent on Polarity Reversal of HVDC Cable Insulation. *IEEE Trans. Dielectr. Electr. Insul.* **2024**, *31*, 58–65. [CrossRef]

https://doi.org/10.3390/app16178536